Environment International 157 (2021) 106801

Contents lists available at ScienceDirect

Environment International

journal homepage: www.elsevier.com/locate/envint

Secondary organic aerosols produced from photochemical oxidation of secondarily evaporated biomass burning organic gases: Chemical composition, toxicity, optical properties, and climate effect

Zheng Fang [a], Chunlin Li [a], Quanfu He [a], Hendryk Czech [b,c], Thomas Gröger [c], Jianqiang Zeng [d], Hua Fang [d], Shaoxuan Xiao [d], Michal Pardo [a], Elena Hartner [b,c], Daphne Meidan [a], Xinming Wang [d], Ralf Zimmermann [b,c], Alexander Laskin [e,f], Yinon Rudich [a,*]

[a] Department of Earth and Planetary Sciences, Weizmann Institute of Science, Rehovot 76100, Israel
[b] Joint Mass Spectrometry Centre, Chair of Analytical Chemistry, Institute of Chemistry, University of Rostock, 18059 Rostock, Germany
[c] Joint Mass Spectrometry Centre, Comprehensive Molecular Analytics, Helmholtz Zentrum München, 81379 München, Germany
[d] State Key Laboratory of Organic Geochemistry and Guangdong Key Laboratory of Environment Protection and Resources Utilization, Guangzhou Institute of Geochemistry, Chinese Academy of Sciences, Guangzhou 510640, China
[e] Department of Chemistry, Purdue University, West Lafayette, IN 47907, USA
[f] Department of Earth, Atmospheric and Planetary Sciences, Purdue University, West Lafayette, IN 47907, USA

ARTICLE INFO

Handling Editor: Hefa Cheng

Keywords:
Biomass burning
SBB-OGs
SOA
Toxicology response
Brown carbon
Radiative forcing

ABSTRACT

Biomass burning (BB) is an important source of primary organic aerosols (POA). These POA contain a significant fraction of semivolatile organic compounds, and can release them into the gas phase during the dilution process in transport. Such evaporated compounds were termed "secondarily evaporated BB organic gases (SBB-OGs)" to distinguish them from the more studied primary emissions. SBB-OGs contribute to the formation of secondary organic aerosols (SOA) through reactions with atmospheric oxidants, and thus may influence human health and the Earth's radiation budget. In this study, tar materials collected from wood pyrolysis were taken as proxies for POA from smoldering-phase BB and were used to release SBB-OGs constantly in the lab. OH-initiated oxidation of the SBB-OGs in the absence of NO_x was investigated using an oxidation flow reactor, and the chemical, optical, and toxicological properties of SOA were comprehensively characterized. Carbonyl compounds were the most abundant species in identified SOA species. Human lung epithelial cells exposed to an environmentally relevant dose of the most aged SOA did not exhibit detectable cell mortality. The oxidative potential of SOA was characterized with the dithiothreitol (DTT) assay, and its DTT consumption rate was 15.5 ± 0.5 pmol min^{-1} μg^{-1}. The SOA present comparable light scattering to BB-POA, but have lower light absorption with imaginary refractive index less than 0.01 within the wavelength range of 360–600 nm. Calculations based on Mie theory show that pure airborne SOA with atmospherically relevant sizes of 50–400 nm have a cooling effect; when acting as the coating materials, these SOA can counteract the warming effect brought by airborne black carbon aerosol.

1. Introduction

On a global scale, biomass burning (BB) is the main source of primary organic aerosols (POA) (Bond et al., 2004; Huang et al., 2015), and the second-largest source of atmospheric volatile organic compounds (VOCs) (Akagi et al., 2011; Yokelson et al., 2013). VOCs directly emitted from BB (BB-VOCs) contain various oxygenated species (Hatch et al., 2017; Koss et al., 2018), with a high potential to form secondary organic aerosols (SOA) during atmospheric aging (Bruns et al., 2016). Apart from that, a significant fraction of BB-POA constituents are semivolatile (Huffman et al., 2009; May et al., 2013; Hatch et al., 2018), suggesting that they can contribute to SOA formation through evaporation, oxidation, and re-condensation processes (Robinson et al., 2007; Zhao et al., 2014; Sengupta et al., 2020). The massive gap reported in the literature between SOA predicted from the consumed VOC concentrations, and measured SOA (Robinson et al., 2007; Liu et al., 2015b; Deng

* Corresponding author.
E-mail address: yinon.rudich@weizmann.ac.il (Y. Rudich).

https://doi.org/10.1016/j.envint.2021.106801
Received 20 May 2021; Received in revised form 29 June 2021; Accepted 26 July 2021
Available online 31 July 2021

et al., 2017; Fang et al., 2017), can be accounted for by the inclusion of semivolatile organic compounds (SVOCs) and intermediate-volatility organic compounds (IVOCs) reemitted from BB-POA (Hayes et al., 2015; Konovalov et al., 2015). Globally, the amount of SOA formed from BB-S/IVOCs exceeds BB-POA (Tsimpidi et al., 2016), highlighting the importance of this SOA formation pathway. Limited by the diffusion and uptake of oxidants into aerosols, reactions in the particle-phase are often slower than in the gaseous phase. In specific cases, by being transported to the stratosphere, the influence of BB-POA can reach thousands of kilometers in distance and last months in time (Hirsch and Koren, 2021). Hence, POA serves as a reservoir for BB-S/IVOCs that expand their atmospheric lifetime and distribution. BB-S/IVOCs contain a myriad of chemical species, including alcohols, phenols, and polycyclic aromatic hydrocarbons (PAHs) (Kim Oanh et al., 2015; Hatch et al., 2017, 2018; Sengupta et al., 2020). Their gas-particle partitioning is influenced by factors such as species-dependent saturation vapor pressure, temperature, and organic aerosol (OA) concentration (Sengupta et al., 2020), making their emission profiles highly specific to burning and sampling conditions, and thus difficult to establish. Furthermore, studies on SOA formed from atmospheric oxidation reactions of BB-S/IVOCs are scarce.

The burning conditions have a substantial influence on the chemical composition of BB-POA. In flaming-phase combustion, the transformation of biomass into products follows the following stages (Tillman et al., 1981): (1) the biomass fuel is preheated; (2) solid-phase pyrolysis occurs within the fuel, during which volatiles and tar droplets are ejected into the gas phase, and the biomass is transformed into char; (3) gas-phase combustion of volatiles and tar droplets; (4) char combustion. The flame is a high-temperature zone, where semivolatile compounds in tar droplets rapidly evaporate into the gas phase. In contrast, stage three is absent in smoldering-phase BB, and tar droplets are directly emitted as aerosols. As a result, smoldering-phase aerosols have larger potentials to re-emit S/IVOCs than those from flaming-phase aerosols (Huffman et al., 2009). Tar balls from smoldering-phase BB have a typically narrow size distribution peaking at 70–200 nm (Chakrabarty et al., 2010, 2016; Popovicheva et al., 2019), suggesting they can be transported over regional and continental distances. They are also small enough to efficiently penetrate into the human respiratory system. Previous studies have shown that the adverse health effects after exposure to BBOA include inflammatory response, oxidative stress, DNA damage and cell apoptosis (Park et al., 2018; Pardo et al., 2020, 2021). Specifically, Pardo et al. (2020) found that tar droplets emitted from BB can induce oxidative stress responses of mice and the death of human bronchial epithelial cells. When BB takes place indoor for heating or cooking, smokes can touch relatively cold surfaces like the end of exhaust stacks or walls, and considerable BB-POA will stay on those surface and form a layer of tar materials. Those tar materials can slowly re-emit organic gases (OGs) to the indoor environment and then induce the SOA formation. The evolution of bulk BBOA's oxidative stress has been investigated in ambient atmosphere or in OH-initiated reactions (Wong et al., 2019; Li et al., 2021b), while relevant toxicity analyses exclusively on those newly formed SOA hasn't been conducted.

BB is also an important source of absorbing OA, which is termed "brown carbon (BrC)" (Laskin et al., 2015). Using aircraft campaigns and laboratory simulations, a number of studies investigated the evolution of BBOA in the bulk plume, and all found that tens of hours' persistent photochemical aging lowered the absorption of BBOA in the ultraviolet (UV) and visible wavelengths (Bluvshtein et al., 2017; Sumlin et al., 2017; Kumar et al., 2018; Hems et al., 2021). Other experiments investigated the influence of specific factors, such as UV irradiation (Lee et al., 2014; Wong et al., 2017), hydroxyl radical (OH)/nitrate radical (NO_3) initiated heterogeneous oxidation (Li et al., 2019b, 2020b), and evaporation of OA (Hettiyadura et al., 2021; Shetty et al., 2021), on the optical properties of BB-POA. It was concluded that, the evolution of BBOA light absorption depends on both reaction conditions and aging degree. By engulfing around black carbon (BC), the SOA formed from BB-S/IVOCs can influence visibility and radiative forcing. However, relevant studies have not been conducted yet.

Compared to flaming-phase BB, smoldering-phase BB emits larger amounts of POA (Chakrabarty et al., 2010; Sumlin et al., 2018) and has a higher OA enhancement ratio during the aging process (Vakkari et al., 2018), suggesting its important role in accumulating OA mass loading in the air. Pyrolysis is a vital step in smoldering-phase combustion. In this study, wood tar materials collected from wood pellet pyrolysis were used as proxies for smoldering-phase BB-POA (Tóth et al., 2014; Li et al., 2019b, 2020a, 2020b). Secondarily evaporated BB organic gases (SBB-OGs) from BB-POA, which contain a group of often overlooked BB-S/IVOCs, were introduced into an oxidation flow reactor (OFR) to simulate their OH-initiated chemical aging and SOA formation. A suite of advanced online and offline techniques was used for characterizing the chemical composition, toxicity and optical properties of the resulting SOA, following OH-oxidation equivalent to 0.7, 5.5, and 10.6 days of atmospheric exposure in the ambient conditions.

2. Materials and methods

2.1. Generation of SBB-OGs

Wood tar was produced from wood pellet pyrolysis following a procedure described in previous laboratory studies (Tóth et al., 2014; Li et al., 2019b, 2020a, 2020b). Briefly, ~150 g of commercial wood pellets (Hallingdal Trepellets) were heated in a flask at 535 °C in a nitrogen atmosphere, the emitted plume then passed through a water-cooled condenser at 23 °C, and the condensed wood tar material was collected. Under normal atmospheric conditions, the partitioning of organics between the particulate phase and the gas phase is affected by the POA concentration (Robinson et al., 2007), and only SVOCs and specific IVOCs can partition into particles. In this study, the wood tar material condensed on the condenser wall may slightly affect the distribution compared to the atmosphere by promoting condensation of S/IVOCs, and some VOCs. The evaporation of wood tar materials was conducted at a room temperature of 22.5 ± 0.2 °C. The wood tar emulsion was placed in a bubbler operated by N_2 for up to 5 hrs to keep a stable profile of the SBB-OGs.

2.2. OH-initiated reactions in an oxidation flow reactor (OFR)

OH-initiated oxidation of SBB-OGs was conducted in a Potential Aerosol Mass (PAM) OFR (Aerodyne Research Inc., USA) where SOA was generated through homogeneous nucleation and condensation. The PAM reactor works in OFR254-51 mode with principles and operational procedures described elsewhere (Peng et al., 2015; He et al., 2018, 2021; Li et al., 2019b, 2021a). The flow rates of oxygen, dry N_2, and humidified N_2 were set to 0.2, 2.5, and 1.8 L min^{-1}, respectively, resulting in a mean residence time of 151 s and an relative humidity (RH) of 35.7%. The initial concentration of externally supplied O_3 was 51.0 ± 0.2 ppmv. OH exposure (OH_{exp}) was controlled by changing the light intensity of the mercury lamps inside the OFR, and was traced by the decay of SO_2 (Model 43i, Thermo Scientific, USA). OH_{exp} were 9.2×10^{10}, 7.1×10^{11}, and 1.4×10^{12} molecule cm^{-3} s in the three experiments. By assuming an ambient daily average OH concentration of 1.5×10^6 molecule cm^{-3} (Hayes et al., 2013), three experiments simulated equivalent ambient photochemical ages of 0.7, 5.5, and 10.6 days, respectively, which were within the lifetime of specific BB smokes in the atmosphere (e.g. Hirsch and Koren, 2021). For simplicity, the resulting SOA are termed 0.7-days SOA, 5.5-days SOA and 10.6-days SOA hereafter.

As shown in Fig. S1, the output flow from the OFR passed through two ozone scrubbers, one activated carbon tube, and two diffusion dryers filled with silica gel to remove ozone, VOCs and moisture, respectively.

The online chemical composition of the SOA was probed with a high-resolution time-of-flight aerosol mass spectrometer (HR-TOF-AMS; Aerodyne Research Inc., USA) in V mode with a temporal resolution of 1

min. The toolkit Pika 1.16I was used for deriving the SOA composition.

SOA samples with mass loadings of 110, 80, and 390 μg were collected on Teflon filters (47 mm in diameter, 0.2 μm porosity, Omnipore) in experiments with equivalent photochemical ages of 0.7-days, 5.5-days, and 10.6-days, respectively. Collected samples were stored at −20 °C before they were analyzed by thermal desorption - two-dimensional gas chromatography time-of-flight mass spectrometry (TD-GC × GC-TOF MS).

TD-GC × GC-TOF MS, as a powerful technique to unveil the chemical composition and identification of semivolatile species on ambient and combustion aerosols (Schnelle-Kreis et al., 2005; Vogt et al., 2007; Weggler et al., 2014), was performed on a Pegasus® BT 4D GC × GC time-of-flight mass spectrometer (LECO, St. Joseph, MI, USA) equipped with an OPTIC-4 GC inlet system (GL Sciences, Eindhoven Netherlands). Helium was applied as the carrier gas. The GC column set consisted of a SGE™ BPX5 capillary column (5% phenyl polysilphenylene-siloxane, 60 m length, 0.25 mm i.d., 0.25 μm df, SGE, Australia) in the first dimension and a SGE™ BPX50 capillary column (50% phenyl polysilphenylene-siloxane, 1.5 m, 0.1 mm i.d., 0.1 μm df, SGE, Australia) in the second dimension. The temperature for thermal desorption in the OPTIC-4 inlet system was gradually ramped at 2 °C s^{-1} from 40 to 250 °C to introduce the analytes into the GC column. The inlet purge time was 100 sec at a column flow of 1 mL min^{-1} and a split flow of 100 mL min^{-1}. The desorbed compounds were focused via a cryogenic trapping system Cryofocus-4 (GL Sciences, Eindhoven Netherlands) at −100 °C using liquid nitrogen as the coolant media. After holding the initial temperature of 40 °C for 10 min, the primary oven was ramped at 2 °C min^{-1} from 40 °C to 350 °C. The secondary oven was offset by + 20 °C from the primary oven. The MS transfer line temperature was set to 300 °C. Mass acquisition was from 20 to 700 Daltons at 100 Hz. The electron impact energy was 70 eV and the ion source temperature was 250 °C. Punches of each filter were analyzed in triplicates. At the beginning of the sequence and after three subsequent desorptions, blank filters were analyzed. Blank filters and sample filters were spiked with internal standard for quality assurance. Data acquisition was carried out using the vendor-specific ChromaTOF software (LECO, St. Joseph, MI, USA). Details about data processing could be found in Text S1.

2.3. Optical properties of SOA

SOA with at least 6 discrete mobility diameters between 170 and 300 nm were size-selected by an aerodynamic aerosol classifier (AAC, Cambustion Ltd.). The monodisperse SOA were introduced into a broadband cavity enhanced spectrometer (BBCES) in parallel with a cavity ring-down spectrometer (CRDS) at 404 nm and a condensation particle counter (CPC). Detailed descriptions of the BBCES and CRDS systems can be found elsewhere (He et al., 2020). In this study, the BBCES system consisted of two channels that measured light extinction coefficients (α_{ext}) in the wavelength ranges of 313–340 nm and 360–600 nm. The light extinction coefficients at 404 nm were also measured by the CRDS to cross-validate the results obtained by the BBCES retrievals. Using the α_{ext} and the aerosol number concentration (N) measured by CPC, the size- and wavelength-dependent aerosol extinction cross section (σ_{ext}) can be calculated:

$$\sigma_{ext}(\lambda, D_p) = \frac{\alpha_{ext}(\lambda, D_p)}{N} \quad (1)$$

where λ is the wavelength of the incident light and D_p is the particle diameter. Fig. S2 shows that SOA had a spherical and non-porous morphology. In addition, size-dependent analyses from the AMS showed that the SOA maintained a homogeneous chemical composition across different particle sizes (Fig. S3). Therefore, the use of Lorenz-Mie theory to determine their optical properties is justified. Using the measured σ_{ext} of SOA for at least six mobility diameters between 170 and 300 nm, the best refractive index (RI = $n + ki$) that minimizes the size-weighted difference between measurements and calculations can be retrieved for both BBCES and CRDS (Washenfelder et al., 2013).

The light absorption properties of SOA samples were also characterized with UV–Vis spectroscopy (model USB 650, Ocean Optics). Previous studies have shown that airborne BrC has a wide range of polarities, and extraction of BrC in solutions with different polarities resulted in different light absorption values (Lin et al., 2017; Huang et al., 2020). In this study, methanol (purity ≥ 99.9, Sigma-Aldrich) and deionized water (18.2 MΩ) were separately used to extract the SOA from the filters. With each solvent, the soluble SOA was extracted from 1/4 of the filter by vortex shaking (Vortex Genie-2, Scientific Industries) for 20 min. After the solution was removed, the filter was re-extracted using the same procedure to ensure completeness of extraction. Then, collected solutions from extracts were mixed together and filtered through a syringe filter (GHP Acrodisc, 0.45 μm porosity, Pall Life Science) before three repeated UV–Vis absorption measurements at a wavelength range of 300–450 nm.

Assuming that chromophores can be fully extracted by methanol (the reasonability of the assumption is discussed in Text S2), the wavelength-dependent mass absorption coefficient (MAC(λ)) of SOA was first calculated and then converted to the imaginary part of the RI (k) using the following relationships (Laskin et al., 2015):

$$\mathrm{MAC}(\lambda) = \frac{\mathrm{Abs}(\lambda)\cdot \mathrm{In}(10)}{\mathrm{C}\cdot 1} \quad (2)$$

$$\mathrm{k}(\lambda) = \frac{\lambda\cdot\rho\cdot\mathrm{MAC}(\lambda)}{4\pi} \quad (3)$$

where Abs (λ) is the base-10 absorption obtained by the UV–Vis spectrometer, C is the mass concentration of the SOA in the solution, and l is the optical length.

The spectral dependence of light absorption can be fitted by the power-law relationship:

$$\mathrm{MAC}(\lambda) = \mathrm{K}\cdot\lambda^{-\mathrm{AAE}} \quad (4)$$

where K is a constant and AAE is the absorption Ångstöm exponent.

2.4. Effect of SOA on cell viability and its oxidative potential (OP)

The experiment in which SBB-OGs were oxidized with an OH_{exp} equivalent to 10.6-days photochemical aging in the ambient condition was triplicated, in order to collect enough SOA on filters for the toxicity analyses.

First, the cytotoxicity of SOA was tested by measuring the viability of lung epithelial cells to SOA extracts. One entire filter, which was loaded with 150 μg of SOA, was extracted with 6 mL of deionized water. Since the dissolved amount of SOA in water is unknown, an effective concentration of SOA of 25 mg L^{-1} was assigned as an upper limit. Two types of human lung epithelial cells (A549 and Calu-3) were exposed to the water extracts of SOA in vitro. The cell viability after incubation for 24 hrs was taken as an indicator of SOA cytotoxicity. The cell viability was measured by the DNA-intercalating dye propidium iodide using flow cytometry. More detailed descriptions of the method can be found in Text S3.

Second, the OP of SOA was measured by the dithiothreitol (DTT) assay (Cho et al., 2005). Methanol was used to extract SOA with the undissolved particles not filtered, in order to measure the total OP of SOA (Zhu et al., 2020). The consumption rate of DTT for the SOA sample at pH = 7.4 and T = 37 °C was measured by UV–Vis spectroscopy, with detailed procedures summarized in Text S4. The blank experiments were done based on a clean filter with the same procedures. The OP measurements of both the SOA sample and the blank sample were duplicated.

3. Results and discussion

3.1. Chemical composition of SOA generated from SBB-OGs

3.1.1. AMS results

A representative 0.7-days SOA spectrum obtained from AMS and its evolution upon SOA aging are presented in Fig. 2a and Fig S4. Ions were grouped into C_xH_y, C_xH_yO, $C_xH_yO_{>1}$ and $C_xH_yO_zN$ families (x, y, z ≥ 1), according to their oxygen and nitrogen contents. For the 0.7-days SOA, the C_xH_yO and $C_xH_yO_{>1}$ families together constituted 66.2% of the total signal, indicating that the majority of compounds were oxygenated. The nitrogen-containing family $C_xH_yO_zN$ accounted for only 3.1% of the total signal. The most prominent ion CO_2^+ consisted of fragments of acids, esters, and acyl peroxides (Ng et al., 2010, 2011); the abundant ions CHO^+, CH_2O^+, $C_2H_3O^+$, and $C_2H_2O^+$ likely originated from non-acidic oxygenates like aldehydes and ketones (Ng et al., 2011); each of the hydrocarbon-like ions CH_3^+, $C_2H_2^+$, $C_2H_3^+$, and $C_3H_3^+$ had a relative abundance of>3%, with different degrees of unsaturation resulting from the complexity of their parent compounds. The oxidation state of carbon ($OS_c = 2 \times O/C\text{-}H/C$) and the relative abundance of m/z 44 (f_{44}) reached values of 0.12 ± 0.01 and 0.18 (Table 1), respectively, which place the SOA between semivolatile oxygenated OA (SV-OOA) and low-volatility oxygenated OA (LV-OOA) in ambient air (Ng et al., 2010; Kroll et al., 2011).

By comparing normalized spectra (Fig. 2b), a significant increase in carboxylic acids ($m/z = 44$) and a decline in hydrocarbon-like ions C_xH_y can be seen from the 0.7-days to 5.5-days SOA. Upon aging, the OS_c increased to 0.49 and f_{44} reached 0.22 in the 5.5-days SOA, typical of LV-OOA or highly aged BBOA in the ambient atmosphere (Cubison et al., 2011; Liang et al., 2021). From the 5.5-days to 10.6-days SOA, the fraction of C_xH_yO fragments decreased from 40.2% to 37.7%, while the proportion of the $C_xH_yO_{>1}$ family increased from 32.2% to 36.0% (Fig. 2c), indicating that the further oxidation added more oxygen to the first-generation products (Lambe et al., 2012). The increases in both OS_c and f_{44} were slower in this aging stage compared to the earlier one, consistent with a study on the urban air (Liu et al., 2018). The OS_c (0.65 ± 0.02) and f_{44} (0.250) of the 10.6-days SOA were still in the range of LV-OOA or highly aged BBOA observed in the ambient atmosphere.

3.1.2. TD-GC × GC MS results

A total of ~2300 peaks with signal-to-noise ratios >2500 were observed in the TD-GC × GC-TOF-MS spectra. The desorption temperature was limited to 250 °C to avoid excessive pyrolysis of temperature-sensitive compounds. For the given desorption and chromatographic conditions, we observed compounds with vapor pressure ranging between octane and triacontane, which correspond mainly to semivolatile species. For SOA derived from three photochemical ages, the 100 most abundant species were analyzed in detail. Based on similarities of their mass spectra to the NIST library spectra, their retention time, and the reasonability of the proposed structure, 59 compounds were assigned with molecular structures. These species generate 58% of the total detected signal on average, and their full list is included in Fig. S5. Most of them showed elution time that ranged between *n*-octane and *n*-pentadecane in the first GC dimension.

As shown in Fig. 1, identified semivolatile compounds were classified into six categories according to their functionality and structure. SOA with a photochemical age of at least 5.5 days still contained specific hydrocarbons, such as toluene or styrene, which cannot be formed during photochemical oxidation and were expected to be completely degraded due to their OH reactivity. Grabowsky et al. (2011) and Diab et al. (2015) observed thermal breakdown in BB-impacted ambient particle samples when the desorption temperature was set at 250–450 °C and 280 °C, respectively. Therefore, those hydrocarbons may be produced from decomposition of larger components during thermal desorption.

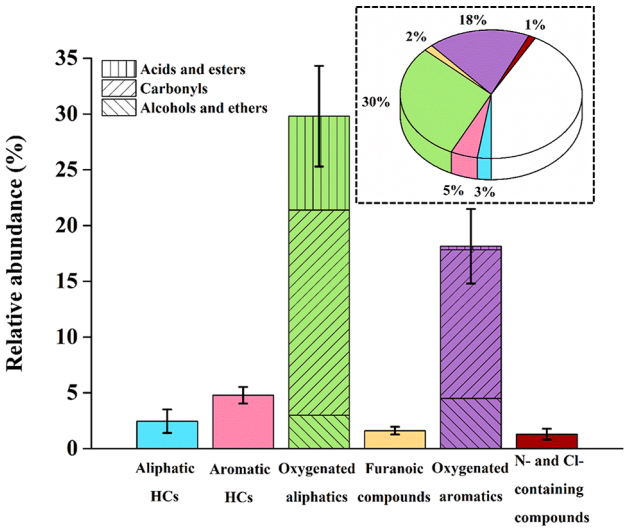

Fig. 1. The relative abundances of different classes of identified semivolatile species in SOA. Oxygenated aliphatics and aromatics are further classified into three subtypes according to their functionalities. The white sector in the inset comprises the remaining species which were either less abundant or difficult to be identified. Error bars correspond to the uncertainty of summed values in each category.

Consistent with the high OS_c measured by AMS, 85% of identified species were oxygenated. Carbonyl compounds dominated the detected aromatics and aliphatics in SOA. Organic acids are also important oxidation products in BB-SOA (Yazdani et al., 2020), while their proportions may be underestimated in this study, since some of them have lower decomposition temperatures than their boiling temperatures (Fortenberry et al., 2018).

The identified ring-retaining aromatics contributed 23% of the total signal in SOA samples. Specific identified aromatics in SOA have been described in the literature as oxidation products of PAHs. For example, 1,4-dihydronaphthalene and derivatives of the phthalic acid can be the ring-retaining and ring-opening products of naphthalene, respectively (Kautzman et al., 2010). However, ring-retaining products of PAHs with 3 or more rings were found in trace amounts. PAHs with more rings usually have lower volatility, thus one possible reason is that their oxidation products cannot be efficiently analyzed at the thermal desorption temperature of less than 250 °C.

ANOVA analysis and hierarchical clustering were used to discriminate semivolatile compounds detected in SOA with different photochemical ages (Fig. S6 and S7). The applied statistical methods allowed us to discriminate the aging conditions based on the found peaks. However, limited by the thermal decomposition of certain compounds, the volatility range of gas chromatography, and the number of compounds that can be unambiguously identified, the results may be biased.

Table 1
Elemental ratios, f_{43} and f_{44} of SOA obtained from AMS.

	H/C	O/C	OM/OC	OS_c	f_{43}	f_{44}
0.7-days SOA	1.33 ± 0.01	0.73 ± 0.01	2.09 ± 0.01	0.12 ± 0.01	0.09	0.18
5.5-days SOA	1.25 ± 0.01	0.87 ± 0.01	2.28 ± 0.01	0.49 ± 0.02	0.09	0.22
10.6-days SOA	1.21 ± 0.01	0.93 ± 0.01	2.35 ± 0.02	0.65 ± 0.02	0.09	0.25

3.2. Toxicity analyses of SOA

Previous studies have shown that BBOA that were aged in an ambient condition (Wong et al., 2019) and with OH-oxidation (Li et al., 2021b)

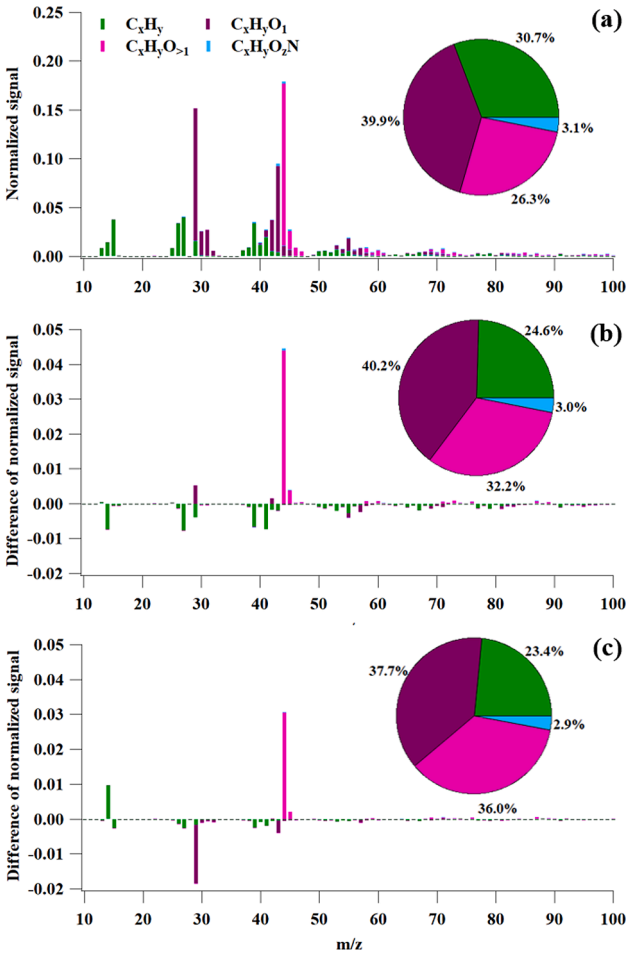

Fig. 2. (a) The AMS spectrum of SOA produced under 0.7-days equivalent OH_{exp} with the total signal normalized to 1.0. (b) The differential normalized AMS spectrum of SOA produced under 5.5-days and 0.7-days equivalent OH_{exp}, with positive values indicating an enrichment under further OH oxidation. (c) The differential normalized AMS spectrum of SOA produced under 10.6-days and 5.5-days equivalent OH_{exp}. The insets in (a), (b) and (c) represent the proportion of each chemical family in 0.7-days, 5.5-days and 10.6-days SOA, respectively. The normalized AMS spectra of 5.5-days and 10.6-days SOA are depicted in Fig. S4.

both increased in OP. In this study, the toxicity of the most aged SOA were examined.

3.2.1. *Lung epithelial cell viability after exposure to water extracts of SOA*

As shown in Fig. S8, for both types of human lung epithelial cells (A549 and Calu-3), no significant differences were observed between the cells treated with different concentrations (0.25 mg L^{-1} and 25 mg L^{-1}) of SOA extracts and the blanks. The equivalent environmental exposures of 0.25 mg L^{-1} × 24 h and 25 mg L^{-1} × 24 h used in our method are estimated to be 2 × 10^2 μg m^{-3} SOA × 24 h and 2 × 10^4 μg m^{-3} SOA × 24 h in the inhaled air (Text S3). Considering that BB events can induce SOA concentration of tens or hundreds of μg m^{-3} in the ambient air, the dose of 2 × 10^2 μg m^{-3} SOA × 24 h can serve as an upper limit for human exposure while the dose of 2 × 10^4 μg m^{-3} SOA × 24 h is two orders of magnitudes larger than that. Therefore, the SOA generated from OH-oxidation of SBB-OGs has no significant cytotoxicity at an environmentally relevant dose. Pardo et al. (2020, 2021) found that 24 h after exposure to 20 mg L^{-1} of water-soluble wood tar extracts, approximately 45% BEAS-2B and 62% A549 cells, stained positive for PI, and were considered dead. Compared to the water-soluble wood tar, SOA generated from SBB-OGs exhibit less toxicity to lung cells.

3.2.2. *OP of SOA*

Duplicate measurements on the consumption rate of DTT for the 10.6-days SOA sample exhibited consistent results (Fig. S9), with an average background-corrected value of 15.5 ± 0.5 pmol min^{-1} μg^{-1}. Such a DTT activity is within the range of those of ambient BB aerosols collected from the Brazilian Amazon (4–148 pmol min^{-1} μg^{-1}, Tuet et al., 2019) and from Greece (5–24 pmol min^{-1} μg^{-1}, Wong et al., 2019). In the absence of NO_x, the DTT activities of SOA generated from aliphatic VOC precursors ranged from 9 to 29 pmol min^{-1} μg^{-1}, while those generated from *m*-xylene and naphthalene were 45 and 149 pmol min^{-1} μg^{-1}, respectively (Tuet et al., 2017). As discussed in Section 3.1, SOA generated from oxidation of SBB-OGs are largely constituted by aliphatic compounds and less by aromatic compounds. Therefore, the result in this study is generally consistent with those reported by Tuet et al. (2017).

3.3. *Optical properties of SOA*

3.3.1. *Real part of the RI*

For the SOA formed under three different OH_{exp}, the real parts of the complex RI (*n*) were retrieved for a wavelength range of 313–600 nm by the BBCES and at 404 nm by the CRD (Fig. 3a). The BBCES and CRD results agreed with each other within their uncertainties, demonstrating a high confidence level of the retrieved data. The *n* of three types of SOA generally had a decreasing trend towards longer wavelengths. The relationship between them can be described by a two-term Sellmeier

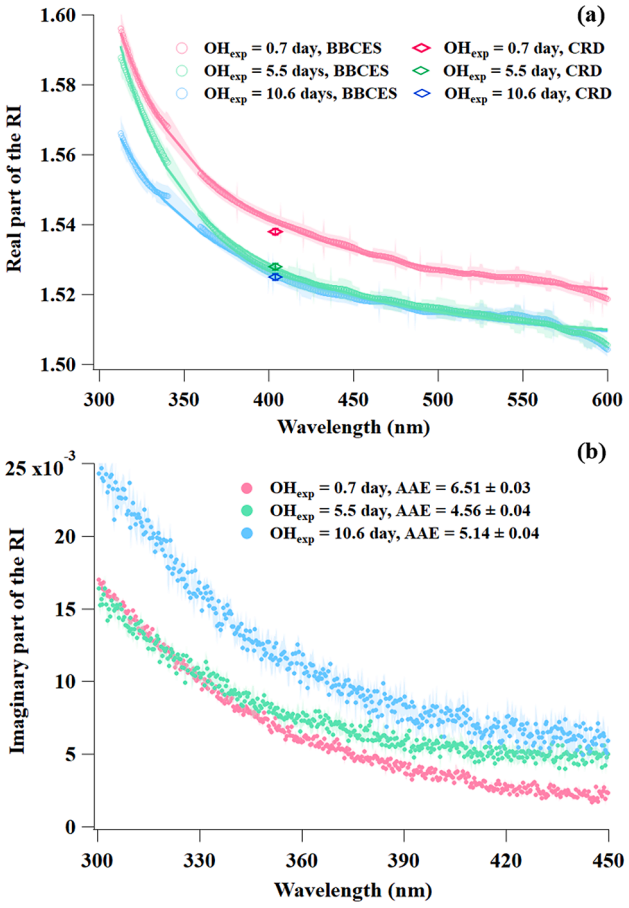

Fig. 3. (a) The real parts of the RI for the 0.7-days, 5.5-days and 10.6-days aged SOA obtained from the BBCES and the CRD-404 nm. For the BBCES retrieval results, the corresponding Sellmeier-equation fitting results are marked by the solid lines. (b) The imaginary parts of the RI for the 0.7-days, 5.5-days, and 10.6-days aged SOA derived by methanol extraction. The uncertainty is denoted by the shaded area.

equation (Ghosh, 1997):

$$n^2 = A + \frac{B_1 \cdot \lambda^2}{\lambda^2 - C_1} + \frac{B_2 \cdot \lambda^2}{\lambda^2 - C_2} \quad (5)$$

where A, B_1, C_1, B_2 and C_2 are Sellmeier coefficients determined from experimental results. As shown in Table 2, all types of OA in this study could be well fitted ($R^2 \geq 0.990$) using the Sellmeier equation. While other equations can also be used to describe the relationship between n and wavelength for aerosols (e.g., Liu et al., 2013; Bluvshtein et al., 2017), one of the advantages of the two-term Sellmeier equation is that the n values outside the measured wavelength range can be well extrapolated for specific materials (Ghosh, 1997). The chromatic dispersion of the n value from 313 nm and 600 nm, denoted as $\Delta n_{313,600}$, was also calculated to indicate the wavelength dependence of n (Liu et al., 2013). Across the studied wavelength range, the n values of the 0.7-days SOA were in the range of 1.519–1.596 with a $\Delta n_{313,600}$ of 0.076. Previous studies have demonstrated that the relationship of SOA oxidation level and n could vary with VOC precursors, reaction conditions and oxidation levels (Flores et al., 2014; Nakayama et al., 2015; He et al., 2018). In this study, continuous declines of the n values for the 5.5-days and 10.6-days SOA were observed (Fig. 3a), with $\Delta n_{313,600}$ first increasing to 0.081 and subsequently decreasing to 0.061.

As shown in Fig. S10a, a comparison was made between n values of SOA obtained in this study and several types of OA in the literature. The n values of SOA in this study are significantly lower than those of the primarily-emitted BBOA from both smoldering duff (Chakrabarty et al., 2010) and wood pyrolysis (Li et al., 2020b). Thus, a decrease in the n value is expected for BB-POA following condensation of such SOA. Peat smoldering POA has comparable n values to those measured in this study, while exhibiting a higher wavelength dependence (Sumlin et al., 2017). For SOA generated from a single or a mixture of BB-VOC precursors, their n values ranged between 1.45 and 1.60 across 313–600 nm, covering the n value range of SOA in this study.

3.3.2. Imaginary part of the RI

Due to low absorption abilities of SOA, the imaginary parts of the RI could not be accurately retrieved from both the BBCES and the CRDS in this study. Alternatively, we applied a solution absorbance method to determine the SOA light absorbing characteristics. As demonstrated in Fig. 3b, the 0.7-days SOA had k values of 0.017 at 300 nm and 0.002 at 450 nm; and the AAE fitted across 300–450 nm was 6.51 ± 0.03. According to the classification by Hettiyadura et al. (2021), the 0.7-day SOA be categorized as "weakly absorbing BrC". Compared with 0.7-days SOA, the 5.5-days SOA had comparable values of k in the short wavelength range (e.g. $k = 0.016$ at 300 nm), but higher k values from ~ 350 nm to 450 nm (e.g. $k = 0.005$ at 450 nm), with the AAE decreasing from 6.51 ± 0.03 to 4.56 ± 0.04. Upon further aging to 10.6-days SOA, the k increased significantly in the UV range (e.g. $k = 0.024$ at 300 nm), while the difference gradually decreased at longer wavelengths, leading to an increase in the AAE to 5.14 ± 0.04. According to the classification by Hettiyadura et al. (2021), SOA generated at all photochemical ages can be categorized as "weakly absorbing BrC". The increase of light absorption goes against the general trend that long-time aging typically photobleach BrC (Hems et al., 2021). When investigating the evolution of BrC absorption during aging, many previous studies include POA in their reaction system (e.g. Sumlin et al., 2017; Kumar et al., 2018; c), while POA were excluded in this study. In the absence of seed aerosols or POA, Lambe et al. (2013) investigated the relationship between oxidation level and light absorption of SOA generated from four separate VOC species, and k values at 405 nm of all types of SOA increased from the lowest to the highest oxidation level, which is consistent of the results in this study.

In addition to methanol, water was also used for BrC extraction with identical procedures. The water-extracted BrC had systematically lower absorbance ($p < 0.01$) than the methanol-extracted BrC for SOA at all ages (Fig. S11), consistent with previous observations of BB-impacted aerosols (Huang et al., 2018; Cao et al., 2021). It is also noted that the difference between the water-soluble BrC and methanol-soluble BrC increased over the aging process, suggesting formation of water-insoluble BrC.

It is evident from Fig. S10b that SOA at all ages in this study have smaller k values than peat smoldering POA (Chakrabarty et al., 2016; Sumlin et al., 2017) and primary wood tar aerosols (Li et al., 2019b). Compared to SOA originating from OH oxidation of a single or a mixture of BB-VOC species, the SOA generated from SBB-OGs in this study are less absorbing than naphthalene-SOA (Xie et al., 2017), but are more absorbing than 1-methylnaphthalene-SOA, 1,2,4-thimethylbenzene-SOA, and m-xylene-SOA in the wavelength range between 300 and 450 nm (Liu et al., 2015a; Xie et al., 2017; Dingle et al., 2019). Other types of SOA in the literature have k values comparable to our SOA at specific wavelengths in the 300–450 nm range. Since the presence of NO_x during aging have been shown to increase light absorption of SOA (Liu et al., 2016), all reference values are all obtained in the absence of NO_x.

3.4. Direct radiative forcing of SOA

3.4.1. Pure SOA: Influence of SOA aging degree and surface albedo

Using the Mie code developed by Bohren and Huffman (1983) and the derived RI, the MAC and mass scattering cross sections (MSC) of pure SOA with an atmospherically relevant size range of 50–400 nm (Betha et al., 2014; Sakamoto et al., 2015; Fang et al., 2017) across a wavelength range of 313–450 nm were obtained (Fig. S12). The single scattering albedo (SSA) can be calculated as:

$$SSA(\lambda) = \frac{MSC(\lambda)}{MSC(\lambda) + MAC(\lambda)} \quad (6)$$

The resulting SSA for SOA at three oxidation levels are depicted in Fig. 4. Upon aging, aerosols generally become less scattering and more absorbing, thus their SSA decrease, shifting the position of the contours towards larger diameters or longer wavelengths. As shown in Table S1, SSA values of SOA in this study are lower than duff smoldering POA, but comparable to or larger than all other types of fresh or aged BBOA.

The simple forcing efficiency (SFE, in W g^{-1} nm^{-1}) is used to evaluate the energy added to the Earth's atmosphere by a unit mass of aerosol (Bond and Bergstrom, 2006). Details of the method to evaluate SFE are summarized in Text S5. The SSA is determined by MAC and MSC, while the parameters that determine whether SFE is positive or negative additionally include the backscatter fraction and surface albedo. Fig. 5a-c presents SFE values for the case of an Earth-average surface albedo of 0.19 (Bond and Bergstrom, 2006). Consistent with the trend that more aged SOA has lower SSA, the area where aerosols exhibit a warming effect expands as SOA is more oxidized. However, even for the 10.6-days SOA, a net cooling effect is expected for the majority of atmospherically relevant aerosols under the irradiation between 313 and 450 nm. Because solar irradiance has a continuous

Table 2
The Sellmeier coefficients describing the wavelength dependence of n, and the differences in n between 313 and 600 nm.

Equivalent photochemical age for SOA(day)	A	B_1	C_1	B_2	C_2	R^2 of fitting	$\Delta n_{313,600}$
0.7	0.71	0.046	6.3×10^4	0.76	84	0.998	0.076
5.5	0.71	0.041	6.8×10^4	0.75	−875	0.995	0.081
10.6	0.70	0.053	5.3×10^4	0.74	−33	0.990	0.061

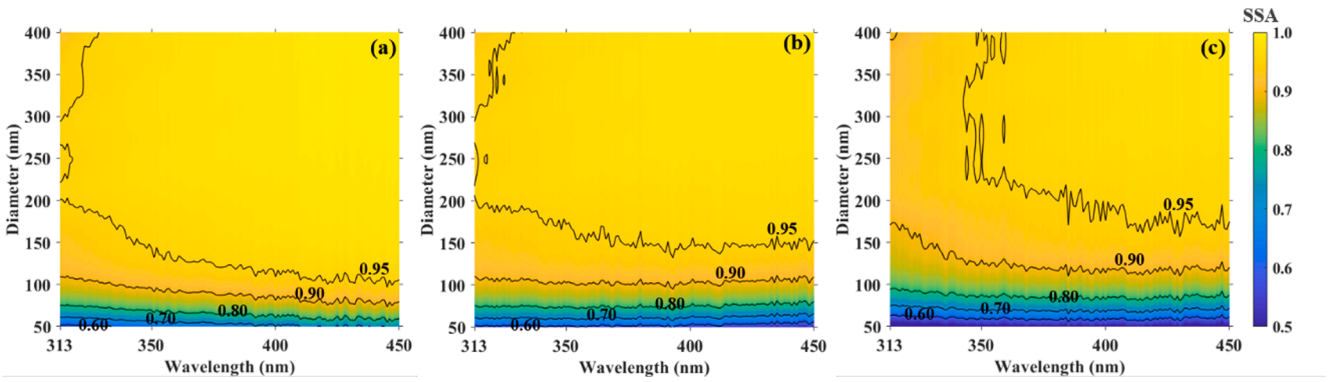

Fig. 4. SSA versus aerosol diameter and wavelength for (a) 0.7-days SOA, (b) 5.5-days SOA, and (c) 10.6-days SOA.

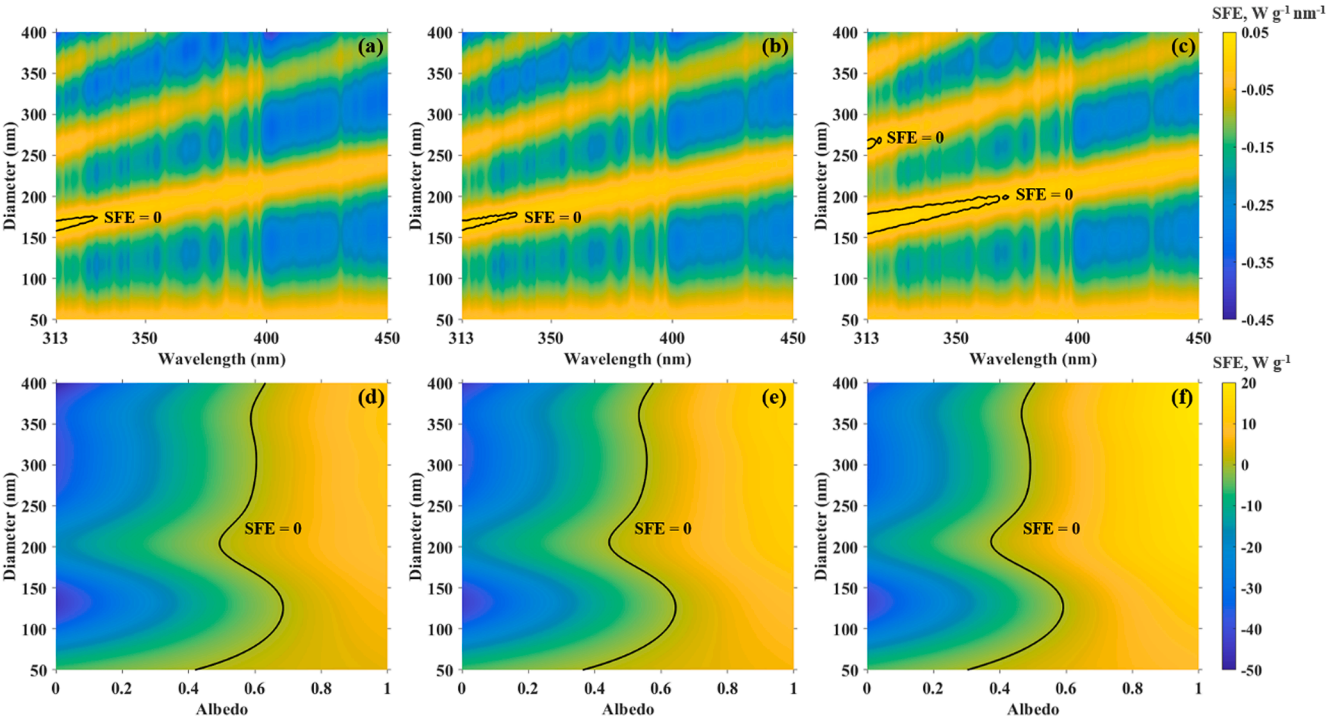

Fig. 5. SFE versus aerosol diameter and wavelength for (a) 0.7-days SOA, (b) 5.5-days SOA, and (c) 10.6-days SOA with a surface albedo = 0.19; the integrated SFE across 313–450 nm against surface albedo and aerosol diameter for (e) 0.7-days SOA, (f) 5.5-days SOA, and (g) 10.6-days SOA.

spectrum, the integrated SFE across 313–450 nm was calculated, and the effects of aerosol diameter and surface albedo are shown in Fig. 5d-f. Across aerosol diameters of 50–400 nm, the average threshold albedos that reach SFE = 0 for the 0.7-days, 5.5-days and 10.6-days SOA are 0.60, 0.55, and 0.49, respectively. Most of non-snow/ice surface types have surface albedos smaller than 0.49 (Jin et al., 2004; Wendisch et al., 2004), so only when suspended above snow or ice-related surfaces (Brandt et al., 2005), a warming effect induced by SOA can be expected. With Eq. (3) and (4), the imaginary part of RI of SOA from 450 nm to 600 nm could be extrapolated, thus the SFE values of SOA at this wavelength range were evaluated. As shown in Fig. S13, a net cooling effect of airborne SOA is still expected beyond non-snow/ice surfaces.

3.4.2. *Internal mixing of SOA and black carbon*

BC, which is a strong absorbing material in primary emissions, has a relatively longer lifetime than POA and thus can be an efficient sinker for SOA. The Mie theory code was used to calculate the optical properties of the internal mixture of SOA and BC, with input parameters summarized in Text S6. SOA coating altered optical properties of BC by enhancing both absorption and scattering. Via sensitivity test assuming a OA/BC mass ratio (R_{BC}) ranging from 0 to 20, the enhancement ratios of BC absorption (E_{abs}, defined by Equation S3) and scattering (E_{sca}, defined by Equation S4) after being coated by SOA ranged between 1.0–4.1 and 1.0–23.9, respectively (Fig. 6). When $R_{BC} > 1$, which represents most cases for ambient BBOA (Liu et al., 2017), E_{sca} is always larger than E_{abs}, suggesting that the coated BC has higher SSA than the pure BC. The effects of the BC core diameter and R_{BC} on the integrated SFE are summarized in Fig. 7, for the case in which the albedo was set to 0.19. Under these conditions, R_{BC} of 2–20 could switch the bulk aerosol from having an originally warming effect to a cooling effect. For aerosols with BC core diameters of 50–400 nm, the average thresholds of R_{BC} to reach SFE = 0 are 5.3, 5.7, and 6.5 for the 0.7-days, 5.5-days, and 10.6-days SOA, respectively.

In ambient conditions, two additional factors need to be considered for the prediction of E_{abs}: (1) when R_{BC} is small, BC is not sufficiently encapsulated by the non-BC material (Liu et al., 2017); (2) R_{BC} exhibits aerosol-to-aerosol variability (Fierce et al., 2016, 2020; Matsui et al., 2018). After taking these two factors into consideration (see Text S7 for

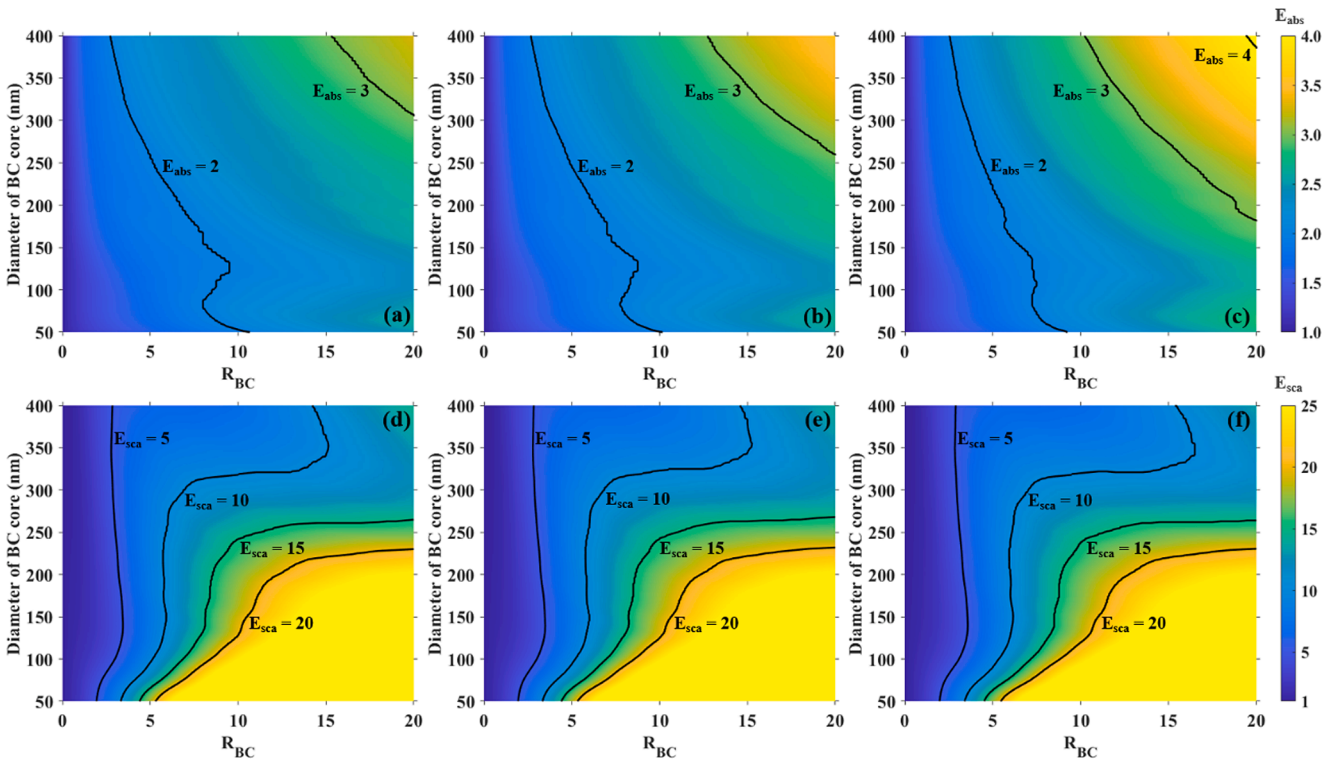

Fig. 6. Light absorption enhancement ratios of BC (E_{abs}) coated by (a) 0.7-days SOA, (b) 5.5-days SOA, and (c) 10.6-days SOA. Light scattering enhancement ratios of BC (E_{sca}) coated by (d) 0.7-days SOA, (e) 5.5-days SOA, and (f) 10.6-days SOA.

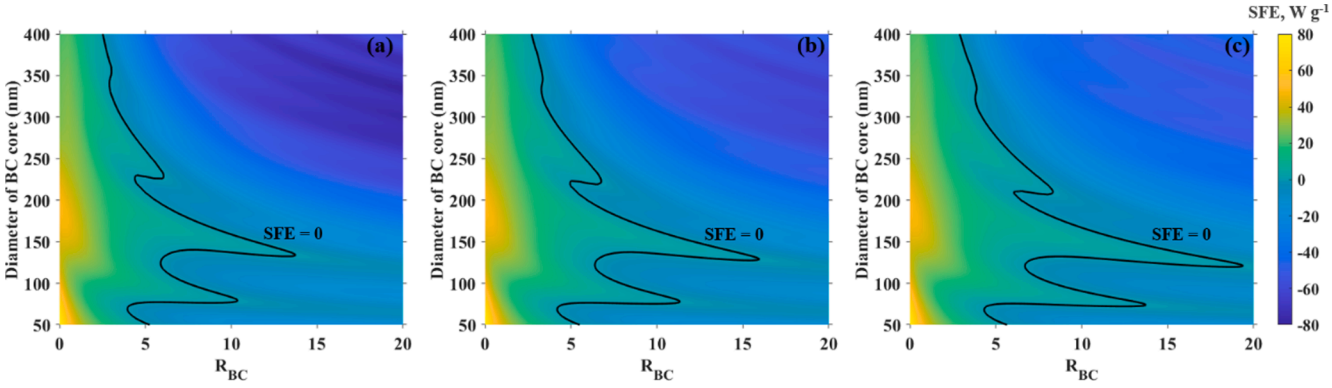

Fig. 7. The integrated SFE against BC diameter and R_{BC} for (a) 0.7-days SOA, (b) 5.5-days SOA, and (c) 10.6-days SOA, when an Earth-average albedo of 0.19 is used.

details), an R_{BC} of 8.94 in a typical ambient BB plume will lead to integrated E_{abs} values of 1.93, 1.95 and 2.03 for the 0.7-days, 5.5-days and 10.6-days SOA, respectively. These values are within the E_{abs} range of ~ 1.00–2.27 established in various ambient/lab measurements (Cappa et al., 2019). Specifically, for ambient BB aerosols with R_{BC} of 11, McMeeking et al. (2014) reported an E_{abs} of 1.84 ± 0.31, which is comparable to our results.

4. Conclusions

In this study, evaporation of wood smoldering POA proxies at room temperature and the subsequent OH oxidation of SBB-OGs were simulated in the laboratory. The chemical composition and toxicity of the generated SOA under equivalent OH_{exp} of 0.7 day, 5.5 days, and 10.6 days were characterized. The broadband complex refractive indices of SOA were measured online by BBCES and offline by solution absorbance method. The direct radiative forcing of SOA across the wavelength range of 313–450 nm was evaluated based on the Mie theory calculations.

Semivolatile compounds in SOA were dominated by carbonyl compounds, in both the aliphatics and the aromatics. At doses comparable or higher than common environmental exposures, the 10.6-days SOA showed no significant cytotoxicity to human lung epithelial cells (A549 and Calu-3). Based on the acellular DTT assay, the 10.6-days SOA has an oxidative potential of 15.5 ± 0.5 pmol min^{-1} μg^{-1}, comparable to those of ambient BBOA or SOA generated from OH oxidation of specific aliphatic VOCs. The real parts of the RI for SOA are within the range of 1.50–1.60 across a wavelength range of 313–600 nm, comparable to SOA formed from specific VOC precursors, like toluene and benzene, but are lower than or comparable to BB-POA. SOA generated from all three photochemical ages could be classified as "weakly absorbing BrC" (Hettiyadura et al., 2021), and more aged SOA showed higher absorption abilities. Over non-ice/snow surfaces, all three ages of airborne SOA with diameters between 50 and 400 nm have a cooling effect on the atmosphere. Above the surface with an albedo of the Earth-average value of 0.19, the SOA in this study can counteract the warming effect of BC by coating it. The offset effect becomes stronger with thicker

coating, and will eventually transform the bulk aerosol into having a cooling effect.

In ambient conditions, as the BB plume becomes gradually diluted and oxidized, the chemical composition and size of BBOA will change, which will alter the evaporation rate and chemical composition of SBB-OGs. Palm et al. (2020) reported that both the formation rate of BB-SOA and evolution rate of SOA light absorption varied under different dilution ratios. This study focuses on SOA formed from SBB-OGs that evaporated from BB-POA in the first few hours. In the future, more studies on SBB-OGs from diverse stages of BBOA should be performed, as well as studies of SOA formation under a variety of aging conditions.

CRediT authorship contribution statement

Zheng Fang: Conceptualization, Investigation, Writing - original draft. **Chunlin Li:** Conceptualization, Methodology, Writing - review & editing. **Quanfu He:** Conceptualization, Methodology, Writing - review & editing. **Hendryk Czech:** Methodology, Writing - review & editing. **Thomas Gröger:** Methodology, Writing - review & editing. **Jianqiang Zeng:** Methodology. **Hua Fang:** Methodology. **Shaoxuan Xiao:** Methodology. **Michal Pardo:** Methodology. **Elena Hartner:** Methodology. **Daphne Meidan:** Software. **Xinming Wang:** Funding acquisition. **Ralf Zimmermann:** Funding acquisition. **Alexander Laskin:** Writing - review & editing. **Yinon Rudich:** Conceptualization, Supervision, Writing - review & editing.

Declaration of Competing Interest

The authors declare that they have no known competing financial interests or personal relationships that could have appeared to influence the work reported in this paper.

Acknowledgements

This study was supported by the NSFC-ISF joint research program (grant NO. 3205/19); the Weizmann Institute of Science and Helmholtz Association in the framework of the German-Israeli project “aero-HEALTH Helmholtz International Lab” (grant NO. InterLabs-0005); the international collaboration grant from US National Science Foundation (NSF Grant No. AGS-2039985) and US-Israel Binational Science Foundation (BSF Grant No. 2020656); a SAERI fellowship of the Weizmann Institute of Science. The morphology of SOA were analyzed by Dr. Sydney Cohen at Department of Chemical Research Support, Weizmann Institute of Science.

Appendix A. Supplementary material

Supplementary data to this article can be found online at https://doi.org/10.1016/j.envint.2021.106801.

References

Akagi, S.K., Yokelson, R.J., Wiedinmyer, C., Alvarado, M.J., Reid, J.S., Karl, T., Crounse, J.D., Wennberg, P.O., 2011. Emission factors for open and domestic biomass burning for use in atmospheric models. Atmos. Chem. Phys. 11, 4039–4072. https://doi.org/10.5194/acp-11-4039-2011.

Betha, R., Zhang, Z., Balasubramanian, R., 2014. Influence of trans-boundary biomass burning impacted air masses on submicron particle number concentrations and size distributions. Atmos. Environ. 92, 9–18. https://doi.org/10.1016/j.atmosenv.2014.04.002.

Bluvshtein, N., Lin, P., Flores, J.M., Segev, L., Mazar, Y., Tas, E., Snider, G., Weagle, C., Brown, S.S., Laskin, A., Rudich, Y., 2017. Broadband optical properties of biomass-burning aerosol and identification of brown carbon chromophores. J. Geophys. Res. 122, 5441–5456. https://doi.org/10.1002/2016jd026230.

Bohren, C.F., Huffman, D.R., 1983. Absorption and scattering of light by small particles. John Wiley & Sons.

Bond, T.C., Bergstrom, R.W., 2006. Light absorption by carbonaceous particles: An investigative review. Aerosol Sci. Technol. 40, 27–67. https://doi.org/10.1080/02786820500421521.

Bond, T.C., Streets, D.G., Yarber, K.F., Nelson, S.M., Woo, J.H., Klimont, Z., 2004. A technology-based global inventory of black and organic carbon emissions from combustion. J. Geophys. Res. 109, 43. https://doi.org/10.1029/2003jd003697.

Brandt, R.E., Warren, S.G., Worby, A.P., Grenfell, T.C., 2005. Surface albedo of the antarctic sea ice zone. J. Clim. 18, 3606–3622. https://doi.org/10.1175/JCLI3489.1.

Bruns, E.A., El Haddad, I., Slowik, J.G., Kilic, D., Klein, F., Baltensperger, U., Prevot, A.S. H., 2016. Identification of significant precursor gases of secondary organic aerosols from residential wood combustion. Sci. Rep. 6 https://doi.org/10.1038/srep27881.

Cao, T., Li, M., Zou, C., Fan, X., Song, J., Jia, W., Yu, C., Yu, Z., Peng, P., 2021. Chemical composition, optical properties, and oxidative potential of water- and methanol-soluble organic compounds emitted from the combustion of biomass materials and coal. Atmos. Chem. Phys. Discuss. 2021, 1–47. https://doi.org/10.5194/acp-2021-159.

Cappa, C.D., Zhang, X., Russell, L.M., Collier, S., Lee, A.K.Y., Chen, C.-L., Betha, R., Chen, S., Liu, J., Price, D.J., Sanchez, K.J., McMeeking, G.R., Williams, L.R., Onasch, T.B., Worsnop, D.R., Abbatt, J., Zhang, Q., 2019. Light absorption by ambient black and brown carbon and its dependence on black carbon coating state for two California, USA, cities in winter and summer. J. Geophys. Res. Atmos. 124, 1550–1577. https://doi.org/10.1029/2018jd029501.

Chakrabarty, R.K., Gyawali, M., Yatavelli, R.L.N., Pandey, A., Watts, A.C., Knue, J., Chen, L.W.A., Pattison, R.R., Tsibart, A., Samburova, V., Moosmüller, H., 2016. Brown carbon aerosols from burning of boreal peatlands: microphysical properties, emission factors, and implications for direct radiative forcing. Atmos. Chem. Phys. 16, 3033–3040. https://doi.org/10.5194/acp-16-3033-2016.

Chakrabarty, R.K., Moosmüller, H., Chen, L.-W.-A., Lewis, K., Arnott, W.P., Mazzoleni, C., Dubey, M.K., Wold, C.E., Hao, W.M., Kreidenweis, S.M., 2010. Brown carbon in tar balls from smoldering biomass combustion. Atmos. Chem. Phys. 10, 6363–6370. https://doi.org/10.5194/acp-10-6363-2010.

Cho, A.K., Sioutas, C., Miguel, A.H., Kumagai, Y., Schmitz, D.A., Singh, M., Eiguren-Fernandez, A., Froines, J.R., 2005. Redox activity of airborne particulate matter at different sites in the Los Angeles Basin. Environ. Res. 99, 40–47. https://doi.org/10.1016/j.envres.2005.01.003.

Cubison, M.J., Ortega, A.M., Hayes, P.L., Farmer, D.K., Day, D., Lechner, M.J., Brune, W. H., Apel, E., Diskin, G.S., Fisher, J.A., Fuelberg, H.E., Hecobian, A., Knapp, D.J., Mikoviny, T., Riemer, D., Sachse, G.W., Sessions, W., Weber, R.J., Weinheimer, A.J., Wisthaler, A., Jimenez, J.L., 2011. Effects of aging on organic aerosol from open biomass burning smoke in aircraft and laboratory studies. Atmos. Chem. Phys. 11, 12049–12064. https://doi.org/10.5194/acp-11-12049-2011.

Deng, W., Hu, Q., Liu, T., Wang, X., Zhang, Y., Song, W., Sun, Y., Bi, X., Yu, J., Yang, W., Huang, X., Zhang, Z., Huang, Z., He, Q., Mellouki, A., George, C., 2017. Primary particulate emissions and secondary organic aerosol (SOA) formation from idling diesel vehicle exhaust in China. Sci. Total Environ. 593–594, 462–469. https://doi.org/10.1016/j.scitotenv.2017.03.088.

Diab, J., Streibel, T., Cavalli, F., Lee, S.C., Saathoff, H., Mamakos, A., Chow, J.C., Chen, L. W.A., Watson, J.G., Sippula, O., Zimmermann, R., 2015. Hyphenation of a EC / OC thermal-optical carbon analyzer to photo-ionization time-of-flight mass spectrometry: an off-line aerosol mass spectrometric approach for characterization of primary and secondary particulate matter. Atmos. Meas. Tech. 8, 3337–3353. https://doi.org/10.5194/amt-8-3337-2015.

Dingle, J.H., Zimmerman, S., Frie, A.L., Min, J., Jung, H., Bahreini, R., 2019. Complex refractive index, single scattering albedo, and mass absorption coefficient of secondary organic aerosols generated from oxidation of biogenic and anthropogenic precursors. Aerosol Sci. Technol. 53, 449–463. https://doi.org/10.1080/02786826.2019.1571680.

Fang, Z., Deng, W., Zhang, Y., Ding, X., Tang, M., Liu, T., Hu, Q., Zhu, M., Wang, Z., Yang, W., Huang, Z., Song, W., Bi, X., Chen, J., Sun, Y., George, C., Wang, X., 2017. Open burning of rice, corn and wheat straws: primary emissions, photochemical aging, and secondary organic aerosol formation. Atmos. Chem. Phys. 17, 14821–14839. https://doi.org/10.5194/acp-17-14821-2017.

Fierce, L., Bond, T.C., Bauer, S.E., Mena, F., Riemer, N., 2016. Black carbon absorption at the global scale is affected by particle-scale diversity in composition. Nat. Commun. 7 https://doi.org/10.1038/ncomms12361.

Fierce, L., Onasch, T.B., Cappa, C.D., Mazzoleni, C., China, S., Bhandari, J., Davidovits, P., Fischer, D.A., Helgestad, T., Lambe, A.T., Sedlacek, A.J., Smith, G.D., Wolff, L., 2020. Radiative absorption enhancements by black carbon controlled by particle-to-particle heterogeneity in composition, 201919723 Proc. Natl. Acad. Sci.. https://doi.org/10.1073/pnas.1919723117.

Flores, J.M., Zhao, D.F., Segev, L., Schlag, P., Kiendler-Scharr, A., Fuchs, H., Watne, Å.K., Bluvshtein, N., Mentel, T.F., Hallquist, M., 2014. Evolution of the complex refractive index in the UV spectral region in ageing secondary organic aerosol. Atmos. Chem. Phys. 14 https://doi.org/10.5194/acp-14-5793-2014.

Fortenberry, C.F., Walker, M.J., Zhang, Y.P., Mitroo, D., Brune, W.H., Williams, B.J., 2018. Bulk and molecular-level characterization of laboratory-aged biomass burning organic aerosol from oak leaf and heartwood fuels. Atmos. Chem. Phys. 18, 2199–2224. https://doi.org/10.5194/acp-18-2199-2018.

Ghosh, G., 1997. Sellmeier coefficients and dispersion of thermo-optic coefficients for some optical glasses. Appl. Opt. 36, 1540–1546. https://doi.org/10.1364/AO.36.001540.

Grabowsky, J., Streibel, T., Sklorz, M., Chow, J.C., Watson, J.G., Mamakos, A., Zimmermann, R., 2011. Hyphenation of a carbon analyzer to photo-ionization mass spectrometry to unravel the organic composition of particulate matter on a molecular level. Anal. Bioanal. Chem. 401, 3153–3164. https://doi.org/10.1007/s00216-011-5425-1.

Hatch, L.E., Rivas-Ubach, A., Jen, C.N., Lipton, M., Goldstein, A.H., Barsanti, K.C., 2018. Measurements of I/SVOCs in biomass-burning smoke using solid-phase extraction

disks and two-dimensional gas chromatography. Atmos. Chem. Phys. 18, 17801–17817. https://doi.org/10.5194/acp-18-17801-2018.
Hatch, L.E., Yokelson, R.J., Stockwell, C.E., Veres, P.R., Simpson, I.J., Blake, D.R., Orlando, J.J., Barsanti, K.C., 2017. Multi-instrument comparison and compilation of non-methane organic gas emissions from biomass burning and implications for smoke-derived secondary organic aerosol precursors. Atmos. Chem. Phys. 17, 1471–1489. https://doi.org/10.5194/acp-17-1471-2017.
Hayes, P.L., Carlton, A.G., Baker, K.R., Ahmadov, R., Washenfelder, R.A., Alvarez, S., Rappengluck, B., Gilman, J.B., Kuster, W.C., de Gouw, J.A., Zotter, P., Prevot, A.S.H., Szidat, S., Kleindienst, T.E., Offenberg, J.H., Ma, P.K., Jimenez, J.L., 2015. Modeling the formation and aging of secondary organic aerosols in Los Angeles during CalNex 2010. Atmos. Chem. Phys. 15, 5773–5801. https://doi.org/10.5194/acp-15-5773-2015.
Hayes, P.L., Ortega, A.M., Cubison, M.J., Froyd, K.D., Zhao, Y., Cliff, S.S., Hu, W.W., Toohey, D.W., Flynn, J.H., Lefer, B.L., Grossberg, N., Alvarez, S., Rappenglueck, B., Taylor, J.W., Allan, J.D., Holloway, J.S., Gilman, J.B., Kuster, W.C., De Gouw, J.A., Massoli, P., Zhang, X., Liu, J., Weber, R.J., Corrigan, A.L., Russell, L.M., Isaacman, G., Worton, D.R., Kreisberg, N.M., Goldstein, A.H., Thalman, R., Waxman, E.M., Volkamer, R., Lin, Y.H., Surratt, J.D., Kleindienst, T.E., Offenberg, J. H., Dusanter, S., Griffith, S., Stevens, P.S., Brioude, J., Angevine, W.M., Jimenez, J. L., 2013. Organic aerosol composition and sources in Pasadena, California, during the 2010 CalNex campaign. J. Geophys. Res. 118, 9233–9257. https://doi.org/10.1002/jgrd.50530.
He, Q., Bluvshtein, N., Segev, L., Meidan, D., Flores, J.M., Brown, S.S., Brune, W., Rudich, Y., 2018. Evolution of the complex refractive index of secondary organic aerosols during atmospheric aging. Environ. Sci. Technol. 52, 3456–3465. https://doi.org/10.1021/acs.est.7b05742.
He, Q., Fang, Z., Shoshamin, O., Brown, S.S., Rudich, Y., 2020. Scattering and absorption cross-sections of atmospheric gases in the ultraviolet-visible wavelength range (307–725 nm). Atmos. Chem. Phys. Discuss. 2020, 1–32. https://doi.org/10.5194/acp-2020-941.
He, Q., Tomaz, S., Li, C., Zhu, M., Meidan, D., Riva, M., Laskin, A., Brown, S.S., George, C., Wang, X., Rudich, Y., 2021. Optical properties of secondary organic aerosol produced by nitrate radical oxidation of biogenic volatile organic compounds. Environ. Sci. Technol. 55, 2878–2889. https://doi.org/10.1021/acs.est.0c06838.
Hems, R.F., Schnitzler, E.G., Liu-Kang, C., Cappa, C.D., Abbatt, J.P.D., 2021. Aging of atmospheric brown carbon aerosol. ACS Earth Sp. Chem. 5, 722–748. https://doi.org/10.1021/acsearthspacechem.0c00346.
Hettiyadura, A.P.S., Garcia, V., Li, C., West, C.P., Tomlin, J., He, Q., Rudich, Y., Laskin, A., 2021. Chemical composition and molecular-specific optical properties of atmospheric brown carbon associated with biomass burning. Environ. Sci. Technol. 55, 2511–2521. https://doi.org/10.1021/acs.est.0c05883.
Hirsch, E., Koren, I., 2021. Record-breaking aerosol levels explained by smoke injection into the stratosphere. Science (80-.) 371, 1269–1274. https://doi.org/10.1126/science.abe1415.
Huang, R.-J., Yang, L., Shen, J., Yuan, W., Gong, Y., Guo, J., Cao, W., Duan, J., Ni, H., Zhu, C., Dai, W., Li, Y., Chen, Y., Chen, Q., Wu, Y., Zhang, R., Dusek, U., O'Dowd, C., Hoffmann, T., 2020. Water-insoluble organics dominate brown carbon in wintertime urban aerosol of China: Chemical characteristics and optical properties. Environ. Sci. Technol. 54, 7836–7847. https://doi.org/10.1021/acs.est.0c01149.
Huang, R.J., Yang, L., Cao, J.J., Chen, Y., Chen, Q., Li, Y.J., Duan, J., Zhu, C.S., Dai, W.T., Wang, K., Lin, C.S., Ni, H.Y., Corbin, J.C., Wu, Y.F., Zhang, R.J., Tie, X.X., Hoffmann, T., O'Dowd, C., Dusek, U., 2018. Brown carbon aerosol in urban Xi'an, northwest China: The composition and light absorption properties. Environ. Sci. Technol. 52, 6825–6833. https://doi.org/10.1021/acs.est.8b02386.
Huang, Y., Shen, H.Z., Chen, Y.L., Zhong, Q.R., Chen, H., Wang, R., Shen, G.F., Liu, J.F., Li, B.G., Tao, S., 2015. Global organic carbon emissions from primary sources from 1960 to 2009. Atmos. Environ. 122, 505–512. https://doi.org/10.1016/j.atmosenv.2015.10.017.
Huffman, J.A., Docherty, K.S., Mohr, C., Cubison, M.J., Ulbrich, I.M., Ziemann, P.J., Onasch, T.B., Jimenez, J.L., 2009. Chemically-resolved volatility measurements of organic aerosol from different sources. Environ. Sci. Technol. 43, 5351–5357. https://doi.org/10.1021/es803539d.
Jin, Z., Charlock, T.P., Smith Jr, W.L., Rutledge, K., 2004. A parameterization of ocean surface albedo. Geophys. Res. Lett. 31 https://doi.org/10.1029/2004GL021180.
Kautzman, K.E., Surratt, J.D., Chan, M.N., Chan, A.W.H., Hersey, S.P., Chhabra, P.S., Dalleska, N.F., Wennberg, P.O., Flagan, R.C., Seinfeld, J.H., et al., 2010. Chemical composition of gas- and aerosol-phase products from the photooxidation of naphthalene. J. Phys. Chem. A 114, 913–934. https://doi.org/10.1021/jp908530s.
Kim Oanh, N.T., Tipayarom, A., Bich, T.L., Tipayarom, D., Simpson, C.D., Hardie, D., Sally Liu, L.J., 2015. Characterization of gaseous and semi-volatile organic compounds emitted from field burning of rice straw. Atmos. Environ. 119, 182–191. https://doi.org/10.1016/j.atmosenv.2015.08.005.
Konovalov, I.B., Beekmann, M., Berezin, E.V., Petetin, H., Mielonen, T., Kuznetsova, I.N., Andreae, M.O., 2015. The role of semi-volatile organic compounds in the mesoscale evolution of biomass burning aerosol: a modeling case study of the 2010 mega-fire event in Russia. Atmos. Chem. Phys. 15, 13269–13297. https://doi.org/10.5194/acp-15-13269-2015.
Koss, A.R., Sekimoto, K., Gilman, J.B., Selimovic, V., Coggon, M.M., Zarzana, K.J., Yuan, B., Lerner, B.M., Brown, S.S., Jimenez, J.L., Krechmer, J., Roberts, J.M., Warneke, C., Yokelson, R.J., de Gouw, J., 2018. Non-methane organic gas emissions from biomass burning: identification, quantification, and emission factors from PTR-ToF during the FIREX 2016 laboratory experiment. Atmos. Chem. Phys. 18, 3299–3319. https://doi.org/10.5194/acp-18-3299-2018.
Kroll, J.H., Donahue, N.M., Jimenez, J.L., Kessler, S.H., Canagaratna, M.R., Wilson, K.R., Altieri, K.E., Mazzoleni, L.R., Wozniak, A.S., Bluhm, H., 2011. Carbon oxidation state as a metric for describing the chemistry of atmospheric organic aerosol. Nat. Chem. 3, 133–139. https://doi.org/10.1038/nchem.948.
Kumar, N.K., Corbin, J.C., Bruns, E.A., Massabó, D., Slowik, J.G., Drinovec, L., Močnik, G., Prati, P., Vlachou, A., Baltensperger, U., Gysel, M., El-Haddad, I., Prévôt, A.S.H., 2018. Production of particulate brown carbon during atmospheric aging of residential wood-burning emissions. Atmos. Chem. Phys. 18, 17843–17861. https://doi.org/10.5194/acp-18-17843-2018.
Lambe, A.T., Cappa, C.D., Massoli, P., Onasch, T.B., Forestieri, S.D., Martin, A.T., Cummings, M.J., Croasdale, D.R., Brune, W.H., Worsnop, D.R., Davidovits, P., 2013. Relationship between oxidation level and optical properties of secondary organic aerosol. Environ. Sci. Technol. 47, 6349–6357. https://doi.org/10.1021/es401043j.
Lambe, A.T., Onasch, T.B., Croasdale, D.R., Wright, J.P., Martin, A.T., Franklin, J.P., Massoli, P., Kroll, J.H., Canagaratna, M.R., Brune, W.H., Worsnop, D.R., Davidovits, P., 2012. Transitions from functionalization to fragmentation reactions of laboratory secondary organic aerosol (SOA) generated from the OH oxidation of alkane precursors. Environ. Sci. Technol. 46, 5430–5437. https://doi.org/10.1021/es300274t.
Laskin, A., Laskin, J., Nizkorodov, S.A., 2015. Chemistry of atmospheric brown carbon. Chem. Rev. 115, 4335–4382. https://doi.org/10.1021/cr5006167.
Lee, H.J., Aiona, P.K., Laskin, A., Laskin, J., Nizkorodov, S.A., 2014. Effect of solar radiation on the optical properties and molecular composition of laboratory proxies of atmospheric brown sarbon. Environ. Sci. Technol. 48, 10217–10226. https://doi.org/10.1021/es502515r.
Li, C., He, Q., Fang, Z., Brown, S.S., Laskin, A., Cohen, S.R., Rudich, Y., 2020a. Laboratory insights into the diel cycle of optical and chemical transformations of biomass burning brown carbon aerosols. Environ. Sci. Technol. 54, 11827–11837. https://doi.org/10.1021/acs.est.0c04310.
Li, C., He, Q., Hettiyadura, A.P.S., Käfer, U., Shmul, G., Meidan, D., Zimmermann, R., Brown, S.S., George, C., Laskin, A., Rudich, Y., 2020b. Formation of secondary brown carbon in biomass burning aerosol proxies through NO_3 radical reactions. Environ. Sci. Technol. 54, 1395–1405. https://doi.org/10.1021/acs.est.9b05641.
Li, C., He, Q., Schade, J., Passig, J., Zimmermann, R., Meidan, D., Laskin, A., Rudich, Y., 2019b. Dynamic changes in optical and chemical properties of tar ball aerosols by atmospheric photochemical aging. Atmos. Chem. Phys. 19, 139–163. https://doi.org/10.5194/acp-19-139-2019.
Li, C., Windwer, E., Fang, Z., Nissenbaum, D., Rudich, Y., 2021a. Correcting micro-aethalometer absorption measurements for brown carbon aerosol. Sci. Total Environ. https://doi.org/10.1016/j.scitotenv.2021.146143.
Li, J., Li, J., Wang, G., Ho, K.F., Dai, W., Zhang, T., Wang, Q., Wu, C., Li, L., Li, L.i., Zhang, Q., 2021b. Effects of atmospheric aging processes on in vitro induced oxidative stress and chemical composition of biomass burning aerosols. J. Hazard. Mater. 401, 123750. https://doi.org/10.1016/j.jhazmat.2020.123750.
Liang, Y., Jen, C.N., Weber, R.J., Misztal, P.K., Goldstein, A.H., 2021. Chemical composition of $PM_{2.5}$ in October 2017 Northern California wildfire plumes. Atmos. Chem. Phys. 21, 5719–5737. https://doi.org/10.5194/acp-21-5719-2021.
Lin, P., Bluvshtein, N., Rudich, Y., Nizkorodov, S.A., Laskin, J., Laskin, A., 2017. Molecular chemistry of atmospheric brown carbon inferred from a nationwide biomass burning event. Environ. Sci. Technol. 51, 11561–11570. https://doi.org/10.1021/acs.est.7b02276.
Liu, D.T., Whitehead, J., Alfarra, M.R., Reyes-Villegas, E., Spracklen, D.V., Reddington, C.L., Kong, S.F., Williams, P.I., Ting, Y.C., Haslett, S., Taylor, J.W., Flynn, M.J., Morgan, W.T., McFiggans, G., Coe, H., Allan, J.D., 2017. Black-carbon absorption enhancement in the atmosphere determined by particle mixing state. Nat. Geosci. 10, 184–U132. https://doi.org/10.1038/ngeo2901.
Liu, J., Chu, B., Chen, T., Liu, C., Wang, L., Bao, X., He, H., 2018. Secondary Organic aerosol formation from ambient air at an urban site in Beijing: Effects of OH exposure and precursor concentrations. Environ. Sci. Technol. 52, 6834–6841. https://doi.org/10.1021/acs.est.7b05701.
Liu, J., Lin, P., Laskin, A., Laskin, J., Kathmann, S.M., Wise, M., Caylor, R., Imholt, F., Selimovic, V., Shilling, J.E., 2016. Optical properties and aging of light-absorbing secondary organic aerosol. Atmos. Chem. Phys. 16, 12815–12827. https://doi.org/10.5194/acp-16-12815-2016.
Liu, P., Zhang, Y., Martin, S.T., 2013. Complex refractive indices of thin films of secondary organic materials by spectroscopic ellipsometry from 220 to 1200 nm. Environ. Sci. Technol. 47, 13594–13601. https://doi.org/10.1021/es403411e.
Liu, P.F., Abdelmalki, N., Hung, H.M., Wang, Y., Brune, W.H., Martin, S.T., 2015a. Ultraviolet and visible complex refractive indices of secondary organic material produced by photooxidation of the aromatic compounds toluene and m-xylene. Atmos. Chem. Phys. 15, 1435–1446. https://doi.org/10.5194/acp-15-1435-2015.
Liu, T., Wang, X., Deng, W., Hu, Q., Ding, X., Zhang, Y., He, Q., Zhang, Z., Lu, S., Bi, X., Chen, J., Yu, J., 2015b. Secondary organic aerosol formation from photochemical aging of light-duty gasoline vehicle exhausts in a smog chamber. Atmos. Chem. Phys. 15, 9049–9062. https://doi.org/10.5194/acp-15-9049-2015.
Matsui, H., Hamilton, D.S., Mahowald, N.M., 2018. Black carbon radiative effects highly sensitive to emitted particle size when resolving mixing-state diversity. Nat. Commun. 9, 1–11. https://doi.org/10.1038/s41467-018-05635-1.
May, A.A., Levin, E.J.T., Hennigan, C.J., Riipinen, I., Lee, T., Collett Jr., J.L., Jimenez, J. L., Kreidenweis, S.M., Robinson, A.L., 2013. Gas-particle partitioning of primary organic aerosol emissions: 3. Biomass burning. J. Geophys. Res. 118, 11327–11338. https://doi.org/10.1002/jgrd.50828.
McMeeking, G.R., Fortner, E., Onasch, T.B., Taylor, J.W., Flynn, M., Coe, H., Kreidenweis, S.M., 2014. Impacts of nonrefractory material on light absorption by aerosols emitted from biomass burning. J. Geophys. Res. Atmos. 119, 12,212–272,286. https://doi.org/10.1002/2014JD021750.

Nakayama, T., Sato, K., Tsuge, M., Imamura, T., Matsumi, Y., 2015. Complex refractive index of secondary organic aerosol generated from isoprene/NO_x photooxidation in the presence and absence of SO_2. J. Geophys. Res. Atmos. 120, 7777–7787. https://doi.org/10.1002/2015jd023522.

Ng, N.L., Canagaratna, M.R., Jimenez, J.L., Chhabra, P.S., Seinfeld, J.H., Worsnop, D.R., 2011. Changes in organic aerosol composition with aging inferred from aerosol mass spectra. Atmos. Chem. Phys. 11, 6465–6474. https://doi.org/10.5194/acp-11-6465-2011.

Ng, N.L., Canagaratna, M.R., Zhang, Q., Jimenez, J.L., Tian, J., Ulbrich, I.M., Kroll, J.H., Docherty, K.S., Chhabra, P.S., Bahreini, R., Murphy, S.M., Seinfeld, J.H., Hildebrandt, L., Donahue, N.M., DeCarlo, P.F., Lanz, V.A., Prevot, A.S.H., Dinar, E., Rudich, Y., Worsnop, D.R., 2010. Organic aerosol components observed in Northern Hemispheric datasets from Aerosol Mass Spectrometry. Atmos. Chem. Phys. 10, 4625–4641. https://doi.org/10.5194/acp-10-4625-2010.

Palm, B.B., Peng, Q., Fredrickson, C.D., Lee, B.H., Garofalo, L.A., Pothier, M.A., Kreidenweis, S.M., Farmer, D.K., Pokhrel, R.P., Shen, Y., Murphy, S.M., Permar, W., Hu, L., Campos, T.L., Hall, S.R., Ullmann, K., Zhang, X., Flocke, F., Fischer, E.V., Thornton, J.A., 2020. Quantification of organic aerosol and brown carbon evolution in fresh wildfire plumes. Proc. Natl. Acad. Sci. 117, 29469–29477. https://doi.org/10.1073/pnas.2012218117.

Pardo, M., Li, C., He, Q., Levin-Zaidman, S., Tsoory, M., Yu, Q., Wang, X., Rudich, Y., 2020. Mechanisms of lung toxicity induced by biomass burning aerosols. Part. Fibre Toxicol. 17, 4. https://doi.org/10.1186/s12989-020-0337-x.

Pardo, M., Li, C., Fang, Z., Levin-Zaidman, S., Dezorella, N., Czech, H., Martens, P., Käfer, U., Gröger, T., Rüger, C.P., Friederici, L., Zimmermann, R., Rudich, Y., 2021. Toxicity of water- and organic-soluble wood tar fractions from biomass burning in lung epithelial cells. Chem. Res. Toxicol. 34, 1588–1603. https://doi.org/10.1021/acs.chemrestox.1c00020.

Park, M., Joo, H.S., Lee, K., Jang, M., Kim, S.D., Kim, I., Borlaza, L.J.S., Lim, H., Shin, H., Chung, K.H., Choi, Y.-H., Park, S.G., Bae, M.-S., Lee, J., Song, H., Park, K., 2018. Differential toxicities of fine particulate matters from various sources. Sci. Rep. 8, 17007. https://doi.org/10.1038/s41598-018-35398-0.

Peng, Z., Day, D.A., Stark, H., Li, R., Lee-Taylor, J., Palm, B.B., Brune, W.H., Jimenez, J. L., 2015. HO_x radical chemistry in oxidation flow reactors with low-pressure mercury lamps systematically examined by modeling. Atmos. Meas. Tech. 8, 4863–4890. https://doi.org/10.5194/amt-8-4863-2015.

Popovicheva, O.B., Engling, G., Ku, I.T., Timofeev, M.A., Shonija, N.K., 2019. Aerosol emissions from long-lasting smoldering of boreal peatlands: Chemical composition, markers, and microstructure. Aerosol Air Qual. Res. 19, 484–503. https://doi.org/10.4209/aaqr.2018.08.0302.

Robinson, A.L., Donahue, N.M., Shrivastava, M.K., Weitkamp, E.A., Sage, A.M., Grieshop, A.P., Lane, T.E., Pierce, J.R., Pandis, S.N., 2007. Rethinking organic aerosols: Semivolatile emissions and photochemical aging. Science (80-.). 315, 1259–1262. https://doi.org/10.1126/science.1133061.

Sakamoto, K.M., Allan, J.D., Coe, H., Taylor, J.W., Duck, T.J., Pierce, J.R., 2015. Aged boreal biomass-burning aerosol size distributions from BORTAS 2011. Atmos. Chem. Phys. 15, 1633. https://doi.org/10.5194/acp-15-1633-2015.

Schnelle-Kreis, J., Welthagen, W., Sklorz, M., Zimmerman, R., 2005. Application of direct thermal desorption gas chromatography and comprehensive two-dimensional gas chromatography coupled to time of flight mass spectrometry for analysis of organic compounds in ambient aerosol particles. J. Sep. Sci 28, 1648–1657. https://doi.org/10.1002/jssc.200500120.

Sengupta, D., Samburova, V., Bhattarai, C., Watts, A.C., Moosmüller, H., Khlystov, A.Y., 2020. Polar semivolatile organic compounds in biomass-burning emissions and their chemical transformations during aging in an oxidation flow reactor. Atmos. Chem. Phys. 20, 8227–8250. https://doi.org/10.5194/acp-20-8227-2020.

Shetty, N., Beeler, P., Paik, T., Brechtel, F.J., Chakrabarty, R.K., 2021. Bias in quantification of light absorption enhancement of black carbon aerosol coated with low volatility brown carbon. Aerosol Sci. Technol. 1–16 https://doi.org/10.1080/02786826.2021.1873909.

Sumlin, B.J., Heinson, Y.W., Shetty, N., Pandey, A., Pattison, R.S., Baker, S., Hao, W.M., Chakrabarty, R.K., 2018. UV-Vis-IR spectral complex refractive indices and optical properties of brown carbon aerosol from biomass burning. J. Quant. Spectrosc. Radiat. Transf. 206, 392–398. https://doi.org/10.1016/j.jqsrt.2017.12.009.

Sumlin, B.J., Pandey, A., Walker, M.J., Pattison, R.S., Williams, B.J., Chakrabarty, R.K., 2017. Atmospheric photooxidation diminishes light absorption by primary brown carbon aerosol from biomass burning. Environ. Sci. Technol. Lett. 4, 540–545. https://doi.org/10.1021/acs.estlett.7b00393.

Tillman, D.A., Rossi, A.J., Kitto, W.D., 1981. CHAPTER 4 – The process of wood combustion. In: Tillman, D.A., Rossi, A.J., Kitto, W.D. (Eds.), Wood Combustion. Academic Press, pp. 74–97. https://doi.org/10.1016/B978-0-12-691240-1.50008-7.

Tóth, A., Hoffer, A., Nyirő-Kósa, I., Pósfai, M., Gelencsér, A., 2014. Atmospheric tar balls: aged primary droplets from biomass burning? Atmos. Chem. Phys. 14, 6669–6675. https://doi.org/10.5194/acp-14-6669-2014.

Tsimpidi, A.P., Karydis, V.A., Pandis, S.N., Lelieveld, J., 2016. Global combustion sources of organic aerosols: model comparison with 84 AMS factor-analysis data sets. Atmos. Chem. Phys. 16, 8939–8962. https://doi.org/10.5194/acp-16-8939-2016.

Tuet, W.Y., Chen, Y., Xu, L., Fok, S., Gao, D., Weber, R.J., Ng, N.L., 2017. Chemical oxidative potential of secondary organic aerosol (SOA) generated from the photooxidation of biogenic and anthropogenic volatile organic compounds. Atmos. Chem. Phys. 17, 839–853. https://doi.org/10.5194/acp-17-839-2017.

Tuet, W.Y., Liu, F., de Oliveira Alves, N., Fok, S., Artaxo, P., Vasconcellos, P., Champion, J.A., Ng, N.L., 2019. Chemical oxidative potential and cellular oxidative stress from open biomass burning aerosol. Environ. Sci. Technol. Lett. 6, 126–132. https://doi.org/10.1021/acs.estlett.9b00060.

Vakkari, V., Beukes, J.P., Dal Maso, M., Aurela, M., Josipovic, M., van Zyl, P.G., 2018. Major secondary aerosol formation in southern African open biomass burning plumes. Nat. Geosci. 11, 580–583. https://doi.org/10.1038/s41561-018-0170-0.

Vogt, L., Gröger, T., Zimmermann, R., 2007. Automated compound classification for ambient aerosol sample separations using comprehensive two-dimensional gas chromatography-time-of-flight mass spectrometry. J. Chromatogr. A 1150, 2–12. https://doi.org/10.1016/j.chroma.2007.03.006.

Washenfelder, R.A., Flores, J.M., Brock, C.A., Brown, S.S., Rudich, Y., 2013. Broadband measurements of aerosol extinction in the ultraviolet spectral region. Atmos. Meas. Tech. 6, 861–877. https://doi.org/10.5194/amt-6-861-2013.

Weggler, B.A., Gröger, T., Zimmermann, R., 2014. Advanced scripting for the automated profiling of two-dimensional gas chromatography-time-of-flight mass spectrometry data from combustion aerosol. J. Chromatogr. A 1364, 241–248. https://doi.org/10.1016/j.chroma.2014.08.091.

Wendisch, M., Pilewskie, P., Jäkel, E., Schmidt, S., Pommier, J., Howard, S., Jonsson, H. H., Guan, H., Schröder, M., Mayer, B., 2004. Airborne measurements of areal spectral surface albedo over different sea and land surfaces. J. Geophys. Res. Atmos. 109 https://doi.org/10.1029/2003JD004392.

Wong, J.P.S., Nenes, A., Weber, R.J., 2017. Changes in light absorptivity of molecular weight separated brown carbon due to photolytic aging. Environ. Sci. Technol. 51, 8414–8421. https://doi.org/10.1021/acs.est.7b01739.

Wong, J.P.S., Tsagkaraki, M., Tsiodra, I., Mihalopoulos, N., Violaki, K., Kanakidou, M., Sciare, J., Nenes, A., Weber, R.J., 2019. Effects of atmospheric processing on the oxidative potential of biomass burning organic aerosols. Environ. Sci. Technol. 53, 6747–6756. https://doi.org/10.1021/acs.est.9b01034.

Xie, M., Chen, X., Hays, M.D., Lewandowski, M., Offenberg, J., Kleindienst, T.E., Holder, A.L., 2017. Light absorption of secondary organic aerosol: Composition and contribution of nitroaromatic compounds. Environ. Sci. Technol. 51, 11607–11616. https://doi.org/10.1021/acs.est.7b03263.

Yazdani, A., Dudani, N., Takahama, S., Bertrand, A., Prévôt, A.S.H., El Haddad, I., Dillner, A.M., 2020. Characterization of primary and aged wood burning and coal combustion organic aerosols in environmental chamber and its implications for atmospheric aerosols. Atmos. Chem. Phys. Discuss. 2020, 1–32. https://doi.org/10.5194/acp-2020-924.

Yokelson, R.J., Burling, I.R., Gilman, J.B., Warneke, C., Stockwell, C.E., de Gouw, J., Akagi, S.K., Urbanski, S.P., Veres, P., Roberts, J.M., Kuster, W.C., Reardon, J., Griffith, D.W.T., Johnson, T.J., Hosseini, S., Miller, J.W., Cocker, D.R., Jung, H., Weise, D.R., 2013. Coupling field and laboratory measurements to estimate the emission factors of identified and unidentified trace gases for prescribed fires. Atmos. Chem. Phys. 13, 89–116. https://doi.org/10.5194/acp-13-89-2013.

Zhao, Y.L., Hennigan, C.J., May, A.A., Tkacik, D.S., de Gouw, J.A., Gilman, J.B., Kuster, W.C., Borbon, A., Robinson, A.L., 2014. Intermediate-volatility organic compounds: A large source of secondary organic aerosol. Environ. Sci. Technol. 48, 13743–13750. https://doi.org/10.1021/es5035188.

Zhu, J., Shang, J., Chen, Y., Kuang, Y., Zhu, T., 2020. Reactive oxygen species-related inside-to-outside oxidation of soot particles triggered by visible-light irradiation: Physicochemical property changes and oxidative potential enhancement. Environ. Sci. Technol. 54, 8558–8567. https://doi.org/10.1021/acs.est.0c01150.